MATERIALS SCIENCE

Exploring order parameters and dynamic processes in disordered systems via variational autoencoders

Sergei V. Kalinin[1]*, Ondrej Dyck[1], Stephen Jesse[1], Maxim Ziatdinov[2]*

We suggest and implement an approach for the bottom-up description of systems undergoing large-scale structural changes and chemical transformations from dynamic atomically resolved imaging data, where only partial or uncertain data on atomic positions are available. This approach is predicated on the synergy of two concepts, the parsimony of physical descriptors and general rotational invariance of noncrystalline solids, and is implemented using a rotationally invariant extension of the variational autoencoder applied to semantically segmented atom-resolved data seeking the most effective reduced representation for the system that still contains the maximum amount of original information. This approach allowed us to explore the dynamic evolution of electron beam–induced processes in a silicon-doped graphene system, but it can be also applied for a much broader range of atomic scale and mesoscopic phenomena to introduce the bottom-up order parameters and explore their dynamics with time and in response to external stimuli.

INTRODUCTION

Over the past two decades, scanning transmission electron microscopy (STEM) has emerged as an indispensable tool for exploring materials structure and functionality on the atomic level (*1–4*). Recent advances in aberration correction enabled determining the position of individual atomic columns in three-dimensional (3D) materials (*5*) and single atoms in layered materials (*6, 7*) with picometer-level precision (*8*), enabling visualization of ferroelectric polarization and octahedral tilting fields in perovskites (*9–11*), symmetry-breaking phenomena in complex materials such as ferroelectric relaxors and Kitaev materials (*12*), and strain fields in multicomponent systems or in the presence of structural defects (*13*). Equally impressive are the advances in the spectroscopic modes such as electron energy loss spectroscopy, where advances ranging from single-atom spectroscopy (*14, 15*) to mapping plasmonic excitations and phonons have been demonstrated (*14, 16–21*). Last, 4D-STEM methods now offer a pathway to further increasing the information limit in STEM (*22–24*), providing yet unseen details of atomic-level fields and functionalities (*22, 25–27*).

The intriguing and yet largely unexplored opportunity presented by recent progress in STEM is the exploration of atomic-scale chemical processes, either induced by classical global stimuli like temperature or induced by electron beam (e-beam) irradiation. Notably, e-beam damage in electron microscopy has been known from the earliest days of the field (*28–30*) and is traditionally perceived as a strongly deleterious effect. Minimizing e-beam damage along with increasing the spatial resolution were major factors driving the development of electron microscopy instrumentation. The advent of aberration correction and the potential for atomic-resolution imaging at low voltages that it has unlocked have enabled opportunities toward systematic studies of e-beam–induced reactions. Early examples of these studies include phase transformations in 3D materials (*31–34*) and e-beam–induced radiolysis (*35*). A particularly broad

set of opportunities has emerged with extensive studies of 2D materials, where nearly all atomic units are available for observation (*4*) and multiple studies of vacancy and defect formation (*36–41*) and of uncontrolled and controlled atomic motion (*42–51*) have been reported. Harnessing the e-beam effects on atomic dynamics opened a pathway toward atom by atom manipulation, and recently, homo- and heteroatomic cluster assemblies have been reported (*52–55*).

However, further progress in the field necessitates a quantitative description of e-beam–induced transformations as a necessary step for mapping e-beam–induced reaction networks, comparison with predictive and descriptive theory, and ultimately enabling control of e-beam–induced transformations. In cases where the e-beam–induced changes are localized on a single-atom level, these descriptions are possible using the classical point defect chemistry approach, as demonstrated, for example, by Kirkland and co-workers(*36, 39*) for graphene and Maksov *et al.* (*56*) for layered transition metal dichalcogenides. However, the analysis becomes considerably more complicated in cases where large-scale changes in the connectivity of the chemical bond network occur, including changes in coordination, formation of defect agglomerates, and new phase formation. This is unsurprising because the description of the structure of disordered or partially disordered systems, ranging from amorphous solids to physical systems such as spin and cluster glasses or phase-separated oxides, has remained one of the most complex areas of condensed matter physics (*57–59*).

In chemically ordered systems, i.e., in cases where the chemical bond network is that of an ideal solid, symmetry-breaking phenomena can be effectively analyzed using machine learning tools such as multivariate statistical methods or more complex autoencoder (AE)– or variational AE (VAE)–based approaches. In this case, symmetry-breaking distortions are referenced to the known (from the global average) ideal lattice, allowing for straightforward analysis. Recently, this approach was applied to the structural description of perovskites based on column (*11, 60*) and unit cell (*61*) shape analysis, as well as ferroelectric materials and layered chalcogenides based on the analysis of local atomic neighborhoods (*62*). However, this approach fails when the chemical bonding network is nonperiodic, precluding the unambiguous definition of the high-symmetry state.

[1]Center for Nanophase Materials Sciences, Oak Ridge National Laboratory, Oak Ridge, TN 37831, USA. [2]Computational Sciences and Engineering Division, Oak Ridge National Laboratory, Oak Ridge, TN 37831, USA.
*Corresponding author. Email: sergei2@ornl.gov (S.V.K.); ziatdinovma@ornl.gov (M.Z.)

Here, we explore the applicability of machine learning methods, specifically rotationally invariant VAEs, toward the analysis of chemical transformations in 2D materials under e-beam irradiation (Fig. 1). This approach is underpinned by two concepts, the postulated parsimony of structural descriptors in solids and the expectation of global rotational invariance of the system undergoing chemical transformations. That is to say, this approach is rotationally invariant in the sense that we do not know or prescribe the rotation angle of the local bonding pattern with respect to the image plane and allow for it to change from point to point. We demonstrate that the VAE with rotational invariance enables the effective exploration of the chemical evolution of the system based on local structural changes and may be extended to more complex systems.

RESULTS AND DISCUSSION

As a model system, we explore Si in graphene, which has been extensively studied previously in the context of e-beam atomic manipulation (*45, 46, 48, 49, 51, 52*). The description of the experimental protocol is available in Materials and Methods. The experimental datasets representing the multiple snapshots of the system during atomic manipulation or e-beam–induced decomposition have been analyzed using deep convolutional neural networks (DCNNs) to yield pixel probability maps of the carbon and silicon atoms. Training and tuning of the DCNNs are described in previous publications (*56, 63–66*), and associated codes are freely available as a part of AtomAI package on GitHub (*67*).

An example of the DCNN analysis of dynamic STEM data is shown in Fig. 2. The original STEM image contains clearly visible regions of pristine graphene, regions of agglomerated point defects that may cause rotation and fragmentation with respect to original lattice, multiple holes in the graphene, individual Si atoms (bright dots), and regions of an amorphous Si-containing contamination phase. To analyze the data, we used a fully convolutional CNN with an encoder-decoder type of architecture that takes the raw experimental images and produces images where the values at pixels correspond to their likelihood of corresponding to atoms (*61, 68*). The DCNN was trained using images simulated by a MultiSlice algorithm (*69*) and further augmented by applying random cropping, rotations, flipping, scale jittering, adding Poisson/Gaussian noise, and varying the levels of contrast. It is important to note that the network output can be interpreted as a probability that a specific image pixel belongs to a particular atom class, i.e., pixel-wise semantic analysis has been performed.

The DCNN output is shown in Fig. 2B. Here, clusters corresponding to carbon (blue) and silicon (red) are visible, which can naturally be interpreted as localization of the corresponding atoms. We define the centroids of the clusters as atomic positions as visualized in Fig. 2C. Note that this process is robust and only individual atoms are identified and classified, whereas holes and regions where the graphene is obscured by amorphous contamination are excluded from the analysis. This workflow can be applied to the full dynamic STEM image stack in a fully automated manner, decoding the sequence of frames into time-dependent coordinate arrays for C and Si.

The evolution of the Si-graphene system throughout the dynamic STEM measurements is shown in Fig. 3. Here, we use the DCNN output similar to that in Fig. 2B to illustrate the process. Before the
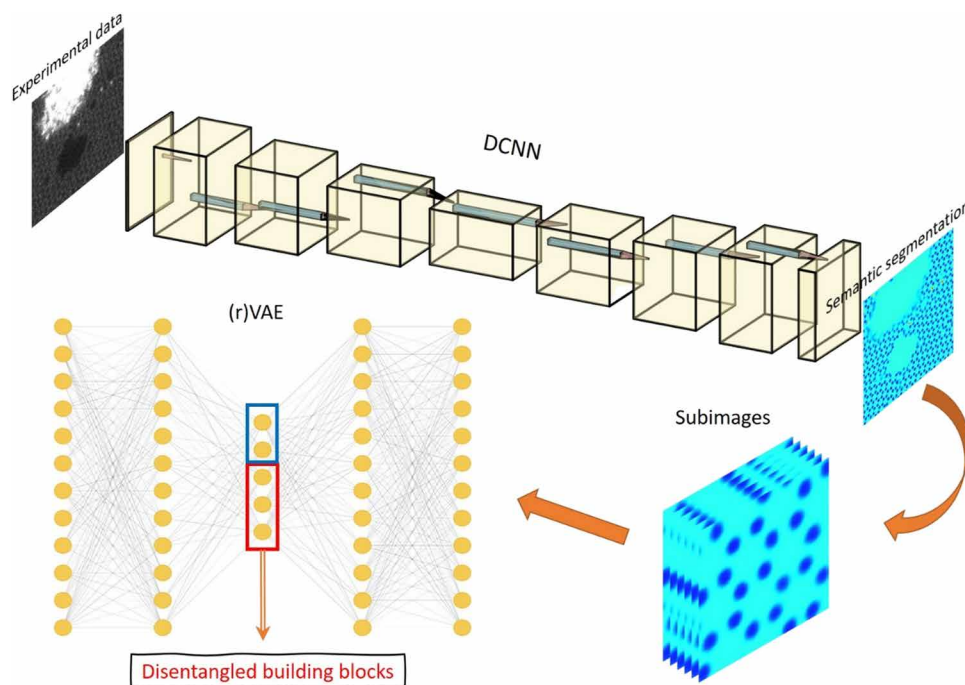
Fig. 1. Schematic of the overall approach. It starts with passing raw experimental data through a pretrained DCNN that categorizes every pixel in the data as belonging to a particular atomic type (e.g., C or Si) or to a "background." The DCNN output is a set of well-defined blobs on a uniform background whose centers correspond to atomic coordinates. Next, a stack of subimages cropped around the identified atomic positions is created and used as an input to a (rotationally invariant) VAE [(r)VAE] that seeks to find the most effective reduced representation for the system (building blocks) that still contains the maximum original information. Here, the three neurons in rotational VAE (rVAE) absorb the information about the rotations and *xy* translations of subimage content, and the other two neurons are used for disentangling the image content itself.
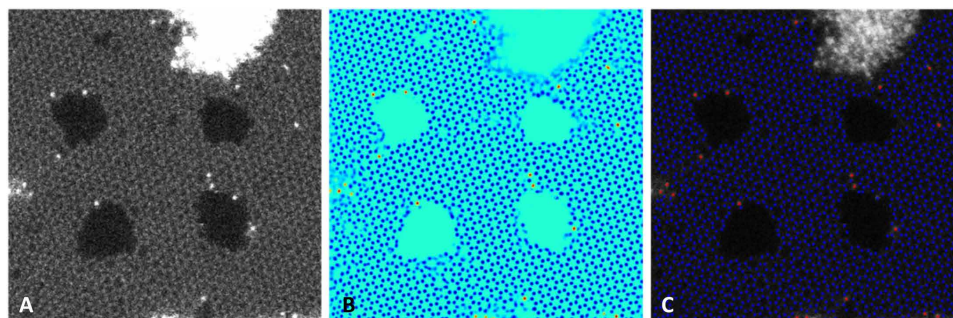
Fig. 2. Experimental and deep learning–processed data. (**A**) Single image from dynamic STEM dataset corresponding to 10th frame. (**B**) DCNN analysis of image in (A) illustrating pixel probability density corresponding to carbon (blue) and silicon (red) atoms. (**C**) Atomic coordinates of C and Si. Note that amorphous region (same as holes) remain unrecognized by the DCNN. Image size is 16 nm.
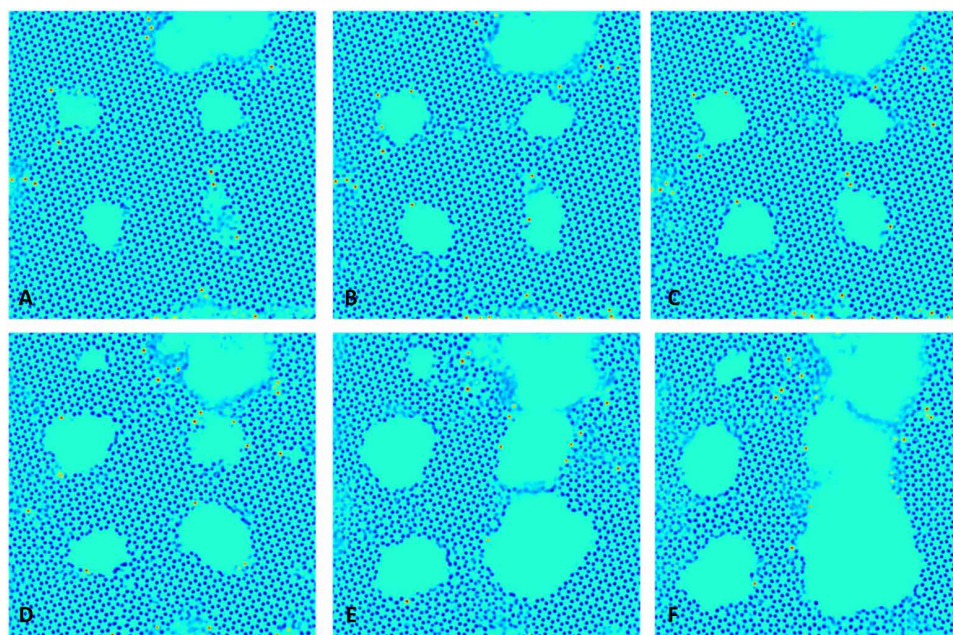
Fig. 3. Evolution of graphene under e-beam irradiation. Images represent DCNN output at (**A**) initial, (**B**) 5th, (**C**) 10th, (**D**) 20th, (**E**) 35th, and (**F**) 49th frame. Red color encodes probability density that specific pixel belongs to Si atom, and blue that it belongs to carbon. Image size is 16 nm.

measurement sequence, several large-scale holes were created using e-beam manipulation to seed the process. On e-beam irradiation, the formation of 5-7 member defect chains from the introduction, diffusion, and accumulation of carbon vacancies is observed (Fig. 3F) (*70*). This process is further associated with growth of the holes and formation of small-angle grain boundaries. The Si atoms tend to migrate during the process and segregate to the edges of the graphene sheet (edges of holes). Overall, the process illustrates changes of the connectivity of C—C and C—Si bond networks during e-beam irradiation.

The dynamic changes observed during the e-beam–induced reactions necessitate the development of suitable descriptors, both to quantify the reaction process and distinguish reaction processes in different settings such as temperature and beam fluency, and ultimately develop strategies for guiding the process through global and local stimuli. Here, the use of classical physical descriptors based on lattice symmetry and symmetry-breaking phenomena is impossible

because the process is associated with the formation and breaking of chemical bonds. At the same time, descriptors based on point defects and clusters in the ideal host lattice also have limited applicability. While individual structural elements such as the formation of 5-7 or 7-5-5-7 defects can be identified, generally, the process associated with the formation of complex defect chains and bonding patterns cannot be uniquely represented as point defects.

Here, we explore the bottom-up description of the process using a machine learning approach where we do not prescribe a priori all of the descriptors; rather, descriptors are determined by prominent patterns within the dataset. Such an approach can be based on several types of descriptors based on the presence of continuous or discrete translational symmetry and initial local structure representation. For uniform sampling used for continuous translational symmetry as shown in Fig. 4A, the subimages are selected and centered on the rectangular grid in the image plane. Subsequent transforms such as fast Fourier transform or Radon transform (depending on the preferred
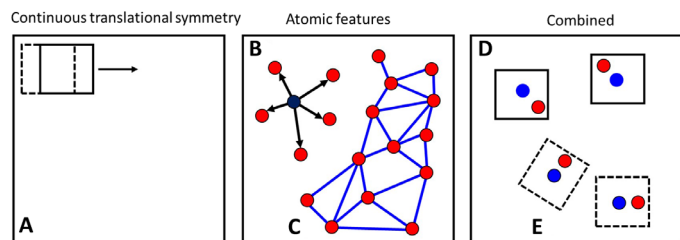
Fig. 4. Defining the building blocks for machine learning based on extant discrete and continuous symmetries in the system. (**A**) In systems with continuous translational symmetry, the initial building blocks can be built using convolution with sliding window and subsequent dimensionality reduction using linear or nonlinear methods. Note that the same principle is used in CNNs. (**B**) In systems with known atomic positions (or other physically defined reference points), the analysis can be performed on the basis of either the local atomic neighborhood of each atom or (**C**) analysis of the connectivity graph between point objects. In this approach, the image is reduced to the coordinates of a small number of features, and remaining information is discarded. Last, local descriptors can be built on the basis of (**D**) continuous neighborhoods of individual atomic units (or other reference point); however, the key element in dimensionality reduction then becomes the presence of (**E**) general rotational symmetry accounting for multiple potentially identical units having different orientations in the image plane.

features) combined with linear or nonlinear unmixing yields the spatial maps of the descriptive parameters (*71–73*). Alternatively, these images can be used as inputs in classical CNNs. This type of analysis is extremely powerful for the detection of patterns such as ferroelectric and magnetic domains, self-assembled monolayers, and atomically resolved images but generally does not take advantage of specific physically defined features within the data such as individual atom positions. Furthermore, it tends to yield a spectrum of descriptors that are amenable only to semiquantitative interpretation.

An alternative set of approaches can be developed for images where atomic positions (or other discrete reference features) are known, naturally extending to the analysis of subimages centered on individual atomic coordinates. In a point representation as introduced in a local crystallography approach, a statistical analysis of the radial vectors to the nearest neighbors is performed (Fig. 4B), enabling classification of local structures (*74, 75*). This analysis can be further extended toward a graphical representation (Fig. 4C). A bonding network can be constructed with the atoms as vertices; the bond strength can be defined as a certain function of atomic spacings and dihedral angles, and graph decomposition methods can be used for deeper analysis. However, this approach relies on the atomic positions being known (or postulated on the basis of a certain threshold level of contrast) and descriptors being the positions of these features. While ideal for theoretical structural datasets, for experimental data, the methods that use partial or uncertain information on the atomic species positions that allow to work with full images and hyperspectral images and using the statistical representations of such distribution will be highly beneficial.

Here, we explore the approach for identification of the individual elements of the chemical bonding network in the material and its evolution during the reaction based on the combined description (Fig. 4, D and E) where the subimages are centered on known atomic positions and the atomic neighborhood is represented as a continuous function defined in the image plane. This approach naturally allows the exploration of images containing both well-defined atomic species and diffuse or uncertain backgrounds. Once the set of subimages

is identified, it naturally brings forth the question of the construction of elementary building blocks or finding a minimal set of descriptors that can represent the full information in the image.

For the system where the chemical bonding pattern does not change, the analysis can be performed using linear dimensionality reduction methods such as principal components analysis or nonnegative matrix factorization, Gaussian mixture model (GMM) separation, or nonlinear methods such as classical AEs and VAEs as explored earlier for local crystallography and FerroNet (*61*) approaches. However, the system that has substantial orientational disorder will not be amenable to these linear methods because the number of classes is no longer fixed and the decomposition components will be dominated by the rotational degrees of freedom and yield smooth distributions of rotational variants. The example of the GMM analysis is shown in the accompanying notebook. Similarly, analysis through the classic AE yields a complex set of descriptors that convolute both the geometry changes and rotations of individual fragments. This results in different descriptors for structures that only differ by virtue of a rotation (i.e., structures that would likely be considered the same), and separating unique geometric configurations from simple rotations becomes challenging.

To address this challenge, we introduce an approach for analyzing the individual building blocks using rotationally invariant VAEs. The classic AE operates on the principle of compressing data to a small number of latent variables and subsequently decoding back to the original dataset. Compression and decoding are typically performed via a set of convolutional filters similar to classical CNNs. The assumption is that if the information can be represented by a small number of latent variables, then variation of these latent variables across the initial dataset provides insight into the relevant physics. In VAE (*76*), one assumes that each point in the dataset is generated by a local random variable in a complex, nonlinear way. The encoder part of a VAE is used to find good values for the latent random variables such that they are true to our (fixed) prior beliefs and true to the data. The priors in a VAE are the type of distribution for the latent variables (usually a Gaussian distribution) and the parameters of this distribution. The decoder part of a VAE is used to make a prediction for the data based on a sample from this distribution. The model parameters (weights and biases) are learned by maximizing the evidence lower bound (ELBO), which consists of the Kullback-Leibler divergence term and the expected likelihood (reconstruction loss). Note that despite the close similarity in names, AEs and VAEs belong to the fundamentally different classes of machine learning algorithms, with VAEs having the Bayesian nature with the latent space defining the priors for the observables. In the absence of prior knowledge, these are chosen as Gaussian (or uniform); however, more complex models are possible in principle (*77*).

Here, the VAE architecture is expanded to account for rotational invariance, which allows rotations to be encoded separately. The implementation of the rotational VAE (rVAE) is based on recent work by Bepler *et al.* (*78*) who showed that parameterization of the VAE's decoder as a function of the image coordinates allows separating the image content from rotations and translations. In this case, the latent variable "layer" contains the rotational angle and two translation vectors as three of the latent variables. Additional latent variables are chosen to represent the variability within the (sub)image content. We found that when using the DCNN output instead of raw data, a simple two-layer perceptron with 128 neurons in each layer of both encoder and decoder is sufficient to learn the

rotationally invariant latent representation of atom-resolved STEM data. For the raw data, the rVAE tends to work better with multiple stacked convolutional layers in the encoder. The encoder and decoder networks are trained jointly, using the Adam optimizer for adjusting weights. As suggested in the original work, the rotational prior was modeled using the Gaussian distribution, with zero mean and an SD of 0.1 radians. The rVAE was trained using 75% of the data, while the remaining 25% were used for testing. The rVAE predictions were made on the entire (0.75 + 0.25) dataset.

Figure 5 shows the analysis of the dataset from Fig. 3 using the GMM, AE, and rVAE methods to contrast the effectiveness of each method. The data are a 3D stack of ~80,000 subimages generated from the 50 initial movie frames. The GMM analysis for a small window (Fig. 5A) generates a set of independent components that can be used to linearly reconstruct the best approximation of the image data. Within these components, we can see that most correspond to partial rotations of the lattice with some variation in intensity. In comparison, a classical AE analysis is illustrated in Fig. 5B where the full variety of the data contained in subimages is reduced to two continuous latent variables represented on the x and y axes. In this case, the elementary building blocks can be visualized in the lattice space. Examination of the data shows that the building blocks corresponding to two carbon sublattice sites are localized in the top left and bottom right corners. Intermediate states occupy the diagonal capturing rotation and other more subtle variations. Again, the primary differentiating factor between the building blocks is rotation and the subtle variations do not have a clear physical interpretation.

These behaviors become even more pronounced for larger numbers of GMM components or larger window sizes (Fig. 5D), which enable a more precise reconstruction of the original data but decrease the physical interpretability. While the GMM effectively determines different components of the dataset from an imaging standpoint, these components are mostly the same from a structural standpoint. If the goal of the analysis is to categorize structural evolution of the sample, then it is not clear how to proceed using the GMM approach.

It could be argued that using only two latent variables in classical AE may be insufficient to describe the variability of the system. For higher–dimensional latent spaces, we adopt the approach where the point distribution corresponding to the real images is clustered via GMM in latent space and the images corresponding to GMM centroids are reconstructed using the decoder part of the AE (*79*). We found that, generally, the reconstructed components also demonstrate the presence of multiple rotation angles. This is unsurprising because changes in the carbon-carbon bond length or geometries are relatively small, whereas transformations associated with the rotation between similar structures are large. In other words, rotations do represent the most pronounced feature within the image data even if the structure is unchanged.

The rVAE analysis is illustrated in Fig. 5 (C and F). Here, the rotations of structural elements are captured in a separate latent variable allowing for their reliable separation from more subtle structural changes. For smaller window size (Fig. 5C), the variability across the latent space in the x direction is due to intensity, which we associate here with a degree of crystallinity (see the next paragraph),
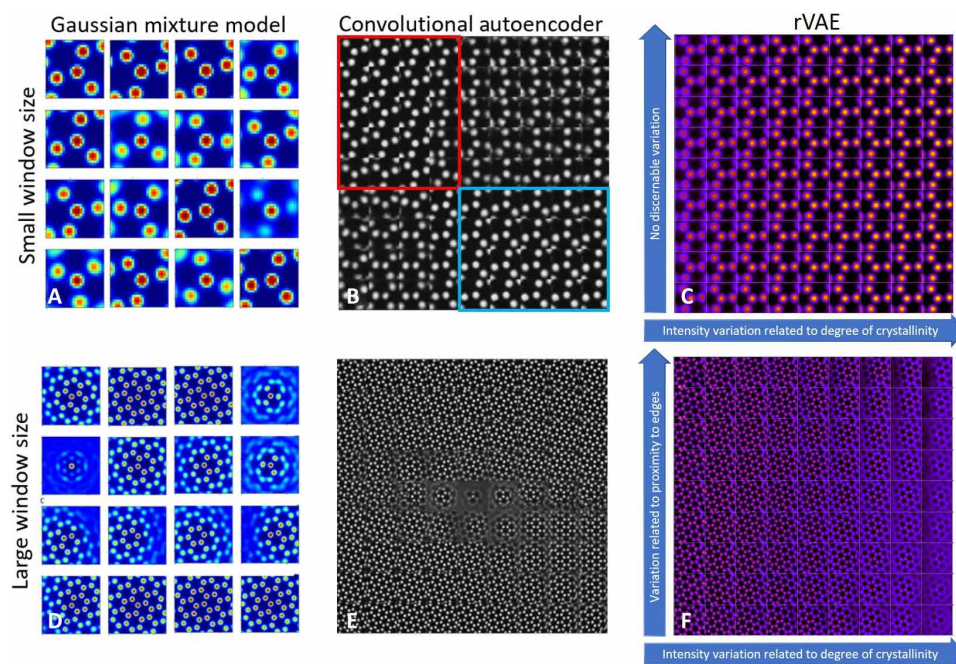
Fig. 5. Comparison of methods for construction of elementary descriptors. (**A** to **C**) small and (**D** to **F**) large windows. (A and D) GMM classes of the data that are decomposed into many independent components that are statistical in nature and often do not allow for direct physical interpretation. In (D), this approach performs poorly at capturing rotation and spreads this information across several components. (B and E) Representation in 2D latent space of convolutional AE. Red and blue regions in (B) indicate clear separation of graphene sublattices with remainder of the descriptors encoding lateral shifts, defects, and rotations in a convoluted fashion. In (E), the larger window introduces variability that is more difficult to interpret. (C and F) Representation in the 2D latent space of rotationally invariant VAE. Because rotational variation is removed from elementary descriptors, remaining variations within data can be described much more efficiently. In (C), there are noticeable changes in only one dimension, which can be ascribed to degree of local crystallinity. In (F), the larger window size also captures variations related to proximity of edges. In (B), (C), (E), and (F), the images were generated by applying a corresponding decoder to the uniform grid of discrete point in the latent space.
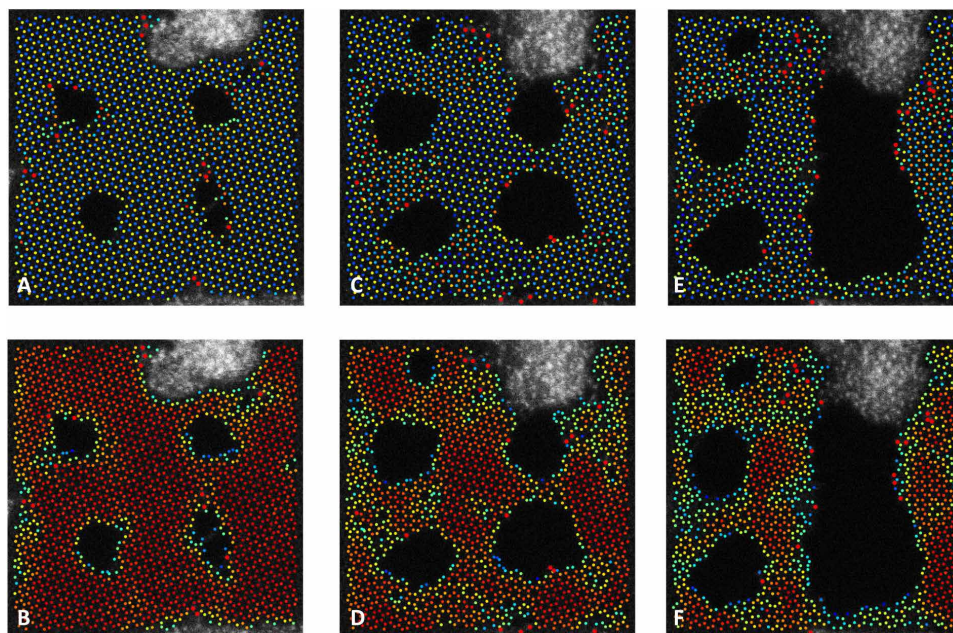
Fig. 6. Real-space visualization of the rVAE's latent variables. Shown are (**A**, **C**, and **E**) angle and (**B**, **D**, and **F**) first latent variable for (A and B) initial, (C and D) 25th, and (E and F) final frame. The positions of Si atoms are indicated by larger red dots. Image size is 16 nm.

and variation along the y direction is minor. A similar analysis can be performed for much larger window sizes as shown in Fig. 5F, demonstrating excellent recovery of structural elements. In this case, one of the latent variables can be interpreted as a degree of crystallinity in the bulk and the other as proximity to the edge of the graphene. The quantitative comparison of GMM, VAE, and rVAE using the structural similarity measure between the unmixed/disentangled structures is shown in fig. S1.

Last, the latent variables can be back-projected to real space to visualize the evolution of the atomic structure, as shown in Fig. 6. Here, the color scale of each atomic unit is set according to the value of the corresponding latent variable for angle (top row) and first latent variable associated with images content (bottom row). The angle variable shows clear contrast for the two structurally unique sublattice positions in the graphene lattice, giving rise to the checkerboard-like pattern. Small-angle boundaries and the rotation between graphene fragments are clearly visible from the color changes in Fig. 6 (C and E). At the same time, the behavior of the latent variable corresponding to the content of subimages clearly shows that it adopts maximum value in the well-ordered regions and is reduced at the edges and in regions with high defect density, allowing for its interpretation as local crystallinity. We were able to reproduce these results even when rVAE was trained using only ~25% of the images from each movie frame and then applied to the entire set.

The time dynamics of the e-beam–induced evolution can be analyzed both in latent space using the time stamp as a parameter and in the time domain. Shown in Fig. 7A is the example of the encoded angle distribution across the whole image stack and (Fig. 7B) its time dependence. Note that the initial sharp bimodal distribution lowers in intensity (because of carbon atom loss) and becomes broader. The evolution of the image latent variables is shown in Fig. 7 (C and D) and demonstrates broadening and reduction in intensity, indicative of lattice decomposition.
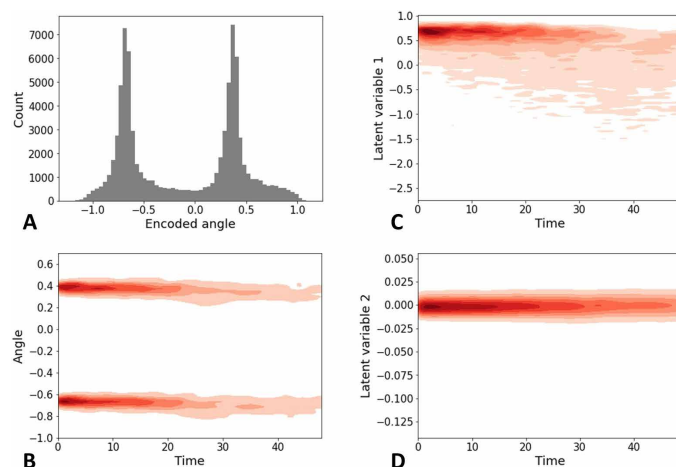
Fig. 7. Time dynamics of the rVAE components. (**A**) Average histogram of angle distribution over the full image stack, (**B**) time-dependent angle distribution, and (**C** and **D**) dynamics of two latent variables associated with image content. Here the angle is given in radians and the time is expressed as the movie frame number.

To summarize, we suggest and implement an approach for the bottom-up description of systems undergoing chemical transformation from atomically resolved imaging data where only partial and uncertain information on atomic positions is available. This approach is predicated on the synergy of two concepts, the parsimony of physical descriptors and the general rotational invariance of noncrystalline solids. The first concept is implemented via the VAE approach, seeking the most effective reduced representation for the system that still contains the maximum original information. The second concept is implementation of rotational invariance. Using this approach, we explore the evolution of e-beam–induced processes in the silicon-graphene system, which can be applied to the studies of

formation of small angle grain boundaries, lattice rotation, and amorphization.

We note that this approach can be applied for a much broader range of atomic-scale and mesoscopic phenomena, including domain dynamics, chemical reactivity, and emergence and dynamics of ordered domains where the natural mechanisms of the process necessitates compensation for the continuous rotation of a structural element. The low–dimensional latent representations yielded by the rVAE provide a bottom-up equivalent of the structural order parameters and hence can be used to describe a broad set of time- and stimulus-dependent phenomena in disordered systems in consistent manner. The code used to analyze data is provided as a Jupyter notebook for the interested readers (https://git.io/JfdSa).

MATERIALS AND METHODS

Sample preparation
Graphene was grown on Cu foil using chemical vapor deposition and spin-coated with poly(methyl methacrylate) (PMMA) to preserve the graphene and provide structural stability during handling. The Cu foil was etched away in an ammonium persulfate bath. The remaining PMMA/graphene stack was rinsed and transferred to a TEM grid, and the PMMA was dissolved in acetone. The sample was baked in a 10% O_2 environment at 500°C for 1.5 hours to remove contaminant residue (80). Before examination in the STEM, the sample was baked again in vacuum at 160°C for 8 hours.

STEM imaging
STEM imaging was performed using a Nion UltraSTEM 200 operated at 100-kV accelerating voltage with a nominal convergence angle of 30 mrad. The high-angle annular dark-field detector was used for imaging with a nominal inner angle of 80 mrad. Four holes were drilled through the pristine graphene using by manually positioning the e-beam. An image stack was then acquired capturing the continued evolution of the four holes under the 100-kV e-beam. The beam current was nominally 20 pA and used a frame acquisition time of ~33.5 s per frame for a dose of 4.2×10^9 electrons per frame.

Data analysis

Deep convolutional neural network
The DCNN for semantic segmentation of atomically resolved images had a U-Net architecture (81) and was trained on simulated data using an Adam optimizer (82) with the cross-entropy loss function and learning rate of 0.001.

Convolutional AE
In the convolutional AE, the encoder had two convolutional layers with 32 and 64 convolutional filters ("kernels") of size (3, 3) and stride (2, 2) activated by a rectified linear unit (ReLU) function. The decoder consisted of two layers with transposed convolutions of the same size and stride activated by ReLU. The latent layer was represented by a fully connected ("dense") layer with two neurons. The model was trained using Adam optimizer with a learning of 0.001 and mean squared error (MSE) loss function.

Gaussian mixture model
For GMM, it is assumed that there are K normal distributions parametrized by their mean (μ_i) and covariance (Σ_i) and that each of extracted subimages $R_i(x, y)$ is independently drawn from one of these distributions with probability density function given by

$$p(\boldsymbol{R}_i) = \frac{1}{(2\pi)^{0.5n} |\Sigma_{k_i}|^{0.5}} \exp\left(-\frac{1}{2}(\boldsymbol{R}_i - \mu_k)^T \Sigma_{k_i}^{-1}(\boldsymbol{R}_i - \mu_k)\right)$$

Here, the number of components is fixed (set by an operator), and the expected minimization algorithm is used to determine the parameters of the mixture.

Rotational variational autoencoder
The generative and inference models of rotationally invariant VAE are parameterized by two deep neural networks, $p_\theta(x|\tau)$ and $q_\phi(\tau|x)$, where θ and ϕ are the parameters (weights and biases) of the neural networks and τ denotes a collective latent variable (image content + translation + rotation). A stochastic gradient descent is used to learn the θ and ϕ parameters via maximizing the ELBO consisting of the MSE term and the Kullback-Leibler divergence terms associated with image content and rotation

$$\begin{aligned} \text{ELBO} = {}&-\text{MSE} - D_{\text{KL}}(q(z|x) \parallel \mathcal{N}(0,I)) - \\ &D_{\text{KL}}(q(\gamma|x) \parallel \mathcal{N}(0,s_\gamma^2)) \end{aligned}$$

where z is a latent variable associated with image content, γ is a latent angle variable, and s_γ is a "rotational prior." Here, we used encoder and decoder both consisting of two fully connected layers with 128 neurons in each layer activated by hyperbolic tangent. The latent layer had three neurons for absorbing arbitrary rotations and translations of images content, whereas the remaining two neurons in the latent layer were used for disentangling the image content. The rVAE was trained using the Adam optimizer with the learning rate of 0.0001.

All deep learning routines were implemented in PyTorch deep learning library (83). For more details, see the interactive Jupyter notebooks reproducing all the data analysis available without restrictions at https://git.io/JfdSa.

SUPPLEMENTARY MATERIALS
Supplementary material for this article is available at http://advances.sciencemag.org/cgi/content/full/7/17/eabd5084/DC1

REFERENCES AND NOTES
1. S. J. Pennycook, P. D. Nellist, in *Scanning Transmission Electron Microscopy: Imaging and Analysis* (Springer, 2011).
2. S. J. Pennycook, M. F. Chisholm, A. R. Lupini, M. Varela, K. van Benthem, A. Y. Borisevich, M. P. Oxley, W. Luo, S. T. Pantelides, in *Advances in Imaging and Electron Physics*, P. W. Hawkes, Ed. (Elsevier Academic Press Inc., 2008), vol. 153, pp. 327–384.
3. P. Y. Huang, S. Kurasch, J. S. Alden, A. Shekhawat, A. A. Alemi, P. L. McEuen, J. P. Sethna, U. Kaiser, D. A. Muller, Imaging atomic rearrangements in two-dimensional silica glass: Watching silica's dance. *Science* **342**, 224–227 (2013).
4. O. L. Krivanek, M. F. Chisholm, V. Nicolosi, T. J. Pennycook, G. J. Corbin, N. Dellby, M. F. Murfitt, C. S. Own, Z. S. Szilagyi, M. P. Oxley, S. T. Pantelides, S. J. Pennycook, Atom-by-atom structural and chemical analysis by annular dark-field electron microscopy. *Nature* **464**, 571–574 (2010).
5. S. Jesse, Q. He, A. R. Lupini, D. N. Leonard, M. P. Oxley, O. Ovchinnikov, R. R. Unocic, A. Tselev, M. Fuentes-Cabrera, B. G. Sumpter, S. J. Pennycook, S. V. Kalinin, A. Y. Borisevich, Atomic-level sculpting of crystalline oxides: Toward bulk nanofabrication with single atomic plane precision. *Small* **11**, 5895–5900 (2015).
6. S. Jesse, B. M. Hudak, E. Zarkadoula, J. Song, A. Maksov, M. Fuentes-Cabrera, P. Ganesh, I. Kravchenko, P. C. Snijders, A. R. Lupini, A. Y. Borisevich, S. V. Kalinin, Direct atomic fabrication and dopant positioning in Si using electron beams with active real-time image-based feedback. *Nanotechnology* **29**, 255303 (2018).
7. B. M. Hudak, J. Song, H. Sims, M. C. Troparevsky, T. S. Humble, S. T. Pantelides, P. C. Snijders, A. R. Lupini, Directed atom-by-atom assembly of dopants in silicon. *ACS Nano* **12**, 5873–5879 (2018).
8. A. B. Yankovich, B. Berkels, W. Dahmen, P. Binev, S. I. Sanchez, S. A. Bradley, A. Li, I. Szlufarska, P. M. Voyles, Picometre-precision analysis of scanning transmission

electron microscopy images of platinum nanocatalysts. *Nat. Commun.* **5**, 4155 (2014).

9. A. Y. Borisevich, H. J. Chang, M. Huijben, M. P. Oxley, S. Okamoto, M. K. Niranjan, J. D. Burton, E. Y. Tsymbal, Y. H. Chu, P. Yu, R. Ramesh, S. V. Kalinin, S. J. Pennycook, Suppression of octahedral tilts and associated changes in electronic properties at epitaxial oxide heterostructure interfaces. *Phys. Rev. Lett.* **105**, 087204 (2010).

10. J. He, A. Borisevich, S. V. Kalinin, S. J. Pennycook, S. T. Pantelides, Control of octahedral tilts and magnetic properties of perovskite oxide heterostructures by substrate symmetry. *Phys. Rev. Lett.* **105**, 227203 (2010).

11. A. Borisevich, O. S. Ovchinnikov, H. J. Chang, M. P. Oxley, P. Yu, J. Seidel, E. A. Eliseev, A. N. Morozovska, R. Ramesh, S. J. Pennycook, S. V. Kalinin, Mapping octahedral tilts and polarization across a domain wall in BiFeO$_3$ from Z-contrast scanning transmission electron microscopy image atomic column shape analysis. *ACS Nano* **4**, 6071–6079 (2010).

12. M. Ziatdinov, A. Banerjee, A. Maksov, T. Berlijn, W. Zhou, H. B. Cao, J. Q. Yan, C. A. Bridges, D. G. Mandrus, S. E. Nagler, A. P. Baddorf, S. V. Kalinin, Atomic-scale observation of structural and electronic orders in the layered compound α-RuCl$_3$. *Nat. Commun.* **7**, 13774 (2016).

13. C. Cantoni, Y. Gao, S. H. Wee, E. D. Specht, J. Gazquez, J. Meng, S. J. Pennycook, A. Goyal, Strain-driven oxygen deficiency in self-assembled, nanostructured, composite oxide films. *ACS Nano* **5**, 4783–4789 (2011).

14. M. Varela, S. D. Findlay, A. R. Lupini, H. M. Christen, A. Y. Borisevich, N. Dellby, O. L. Krivanek, P. D. Nellist, M. P. Oxley, L. J. Allen, S. J. Pennycook, Spectroscopic imaging of single atoms within a bulk solid. *Phys. Rev. Lett.* **92**, 095502 (2004).

15. M. D. Kapetanakis, M. P. Oxley, W. Zhou, S. J. Pennycook, J.-C. Idrobo, S. T. Pantelides, Signatures of distinct impurity configurations in atomic-resolution valence electron-energy-loss spectroscopy: Application to graphene. *Phys. Rev. B* **94**, 155449 (2016).

16. R. F. Egerton, M. Watanabe, Characterization of single-atom catalysts by EELS and EDX spectroscopy. *Ultramicroscopy* **193**, 111–117 (2018).

17. T. Susi, T. P. Hardcastle, H. Hofsäss, A. Mittelberger, T. J. Pennycook, C. Mangler, R. Drummond-Brydson, A. J. Scott, J. C. Meyer, J. Kotakoski, Single-atom spectroscopy of phosphorus dopants implanted into graphene. *2D Materials* **4**, 021013 (2017).

18. Q. M. Ramasse, C. R. Seabourne, D. M. Kepaptsoglou, R. Zan, U. Bangert, A. J. Scott, Probing the bonding and electronic structure of single atom dopants in graphene with electron energy loss spectroscopy. *Nano Lett.* **13**, 4989–4995 (2013).

19. O. L. Krivanek, T. C. Lovejoy, N. Dellby, T. Aoki, R. W. Carpenter, P. Rez, E. Soignard, J. Zhu, P. E. Batson, M. J. Lagos, R. F. Egerton, P. A. Crozier, Vibrational spectroscopy in the electron microscope. *Nature* **514**, 209–212 (2014).

20. O. L. Krivanek, T. C. Lovejoy, N. Dellby, R. W. Carpenter, Monochromated STEM with a 30 meV-wide, atom-sized electron probe. *Microscopy* **62**, 3–21 (2013).

21. O. L. Krivanek, T. C. Lovejoy, M. F. Murfitt, G. Skone, P. E. Batson, N. Dellby, Towards sub-10 meV energy resolution STEM-EELS. *J. Phys. Conf. Ser.* **522**, 012023 (2014).

22. Y. Jiang, Z. Chen, Y. Han, P. Deb, H. Gao, S. Xie, P. Purohit, M. W. Tate, J. Park, S. M. Gruner, V. Elser, D. A. Muller, Electron ptychography of 2D materials to deep sub-angstrom resolution. *Nature* **559**, 343–349 (2018).

23. S. E. Zeltmann, A. Müller, K. C. Bustillo, B. Savitzky, L. Hughes, A. M. Minor, C. Ophus, Patterned probes for high precision 4D-STEM bragg measurements. *Ultramicroscopy* **209**, 112890 (2020).

24. O. Panova, C. Ophus, C. J. Takacs, K. C. Bustillo, L. Balhorn, A. Salleo, N. Balsara, A. M. Minor, Diffraction imaging of nanocrystalline structures in organic semiconductor molecular thin films. *Nat. Mater.* **18**, 860–865 (2019).

25. J. A. Hachtel, J. C. Idrobo, M. Chi, Sub-Ångstrom electric field measurements on a universal detector in a scanning transmission electron microscope. *Adv. Struct. Chem. Imaging* **4**, 10 (2018).

26. X. Li, O. E. Dyck, M. P. Oxley, A. R. Lupini, L. M. Innes, J. Healy, S. Jesse, S. V. Kalinin, Manifold learning of four-dimensional scanning transmission electron microscopy. *npj Comput. Mater.* **5**, 5 (2019).

27. N. Shibata, T. Seki, G. Sánchez-Santolino, S. D. Findlay, Y. Kohno, T. Matsumoto, R. Ishikawa, Y. Ikuhara, Electric field imaging of single atoms. *Nat. Commun.* **8**, 15631 (2017).

28. R. F. Egerton, F. Wang, P. A. Crozier, Beam-induced damage to thin specimens in an intense electron probe. *Microsc. Microanal.* **12**, 65–71 (2006).

29. N. Jiang, Electron beam damage in oxides: A review. *Rep. Prog. Phys.* **79**, 016501 (2016).

30. Z.-L. Wang, N. Itoh, N. Matsunami, Q. T. Zhao, Ion-induced crystallization and amorphization at crystal/amorphous interfaces of silicon. *Nucl. Instrum. Methods Phys. Res. B* **100**, 493–501 (1995).

31. H. M. Zheng, J. B. Rivest, T. A. Miller, B. Sadtler, A. Lindenberg, M. F. Toney, L.-W. Wang, C. Kisielowski, A. P. Alivisatos, Observation of transient structural-transformation dynamics in a Cu$_2$S nanorod. *Science* **333**, 206–209 (2011).

32. T. J. Pennycook, L. Jones, H. Pettersson, J. Coelho, M. Canavan, B. Mendoza-Sanchez, V. Nicolosi, P. D. Nellist, Atomic scale dynamics of a solid state chemical reaction directly determined by annular dark-field electron microscopy. *Sci. Rep.* **4**, 7555 (2014).

33. J. H. Jang, Y. M. Kim, Q. He, R. Mishra, L. Qiao, M. D. Biegalski, A. R. Lupini, S. T. Pantelides, S. J. Pennycook, S. V. Kalinin, A. Y. Borisevich, In situ observation of oxygen vacancy dynamics and ordering in the epitaxial LaCoO$_3$ system. *ACS Nano* **11**, 6942–6949 (2017).

34. J. Lin, O. Cretu, W. Zhou, K. Suenaga, D. Prasai, K. I. Bolotin, N. T. Cuong, M. Otani, S. Okada, A. R. Lupini, J.-C. Idrobo, D. Caudel, A. Burger, N. J. Ghimire, J. Yan, D. G. Mandrus, S. J. Pennycook, S. T. Pantelides, Flexible metallic nanowires with self-adaptive contacts to semiconducting transition-metal dichalcogenide monolayers. *Nat. Nanotechnol.* **9**, 436–442 (2014).

35. P. Abellan, L. R. Parent, N. al Hasan, C. Park, I. Arslan, A. M. Karim, J. E. Evans, N. D. Browning, Gaining control over radiolytic synthesis of uniform sub-3-nanometer palladium nanoparticles: Use of aromatic liquids in the electron microscope. *Langmuir* **32**, 1468–1477 (2016).

36. A. W. Robertson, G. D. Lee, K. He, Y. Fan, C. S. Allen, S. Lee, H. Kim, E. Yoon, H. Zheng, A. I. Kirkland, J. H. Warner, Partial dislocations in graphene and their atomic level migration dynamics. *Nano Lett.* **15**, 5950–5955 (2015).

37. A. W. Robertson, G.-D. Lee, K. He, E. Yoon, A. I. Kirkland, J. H. Warner, Stability and dynamics of the tetravacancy in graphene. *Nano Lett.* **14**, 1634–1642 (2014).

38. A. W. Robertson, G. D. Lee, K. He, E. Yoon, A. I. Kirkland, J. H. Warner, The role of the bridging atom in stabilizing odd numbered graphene vacancies. *Nano Lett.* **14**, 3972–3980 (2014).

39. A. W. Robertson, G.-D. Lee, K. He, C. Gong, Q. Chen, E. Yoon, A. I. Kirkland, J. H. Warner, Atomic structure of graphene subnanometer pores. *ACS Nano* **9**, 11599–11607 (2015).

40. J. Kotakoski, J. C. Meyer, S. Kurasch, D. Santos-Cottin, U. Kaiser, A. V. Krasheninnikov, Stone-wales-type transformations in carbon nanostructures driven by electron irradiation. *Phys. Rev. B* **83**, 245420 (2011).

41. J. Kotakoski, C. Mangler, J. C. Meyer, Imaging atomic-level random walk of a point defect in graphene. *Nat. Commun.* **5**, 3991 (2014).

42. O. Dyck, M. Ziatdinov, D. B. Lingerfelt, R. R. Unocic, B. M. Hudak, A. R. Lupini, S. Jesse, S. V. Kalinin, Atom-by-atom fabrication with electron beams. *Nat. Rev. Mater.* **4**, 497–507 (2019).

43. Z. Yang, L. Yin, J. Lee, W. Ren, H.-M. Cheng, H. Ye, S. T. Pantelides, S. J. Pennycook, M. F. Chisholm, Direct observation of atomic dynamics and silicon doping at a topological defect in graphene. *Angew. Chem.* **126**, 9054–9058 (2014).

44. J. Lee, W. Zhou, S. J. Pennycook, J.-C. Idrobo, S. T. Pantelides, Direct visualization of reversible dynamics in a Si6 cluster embedded in a graphene pore. *Nat. Commun.* **4**, 1650 (2013).

45. O. Dyck, S. Kim, S. V. Kalinin, S. Jesse, Placing single atoms in graphene with a scanning transmission electron microscope. *Appl. Phys. Lett.* **111**, 113104 (2017).

46. O. Dyck, S. Kim, S. V. Kalinin, S. Jesse, E-beam manipulation of Si atoms on graphene edges with an aberration-corrected scanning transmission electron microscope. *Nano Res.* **11**, 6217–6226 (2018).

47. H. Inani, K. Mustonen, A. Markevich, E.-X. Ding, M. Tripathi, A. Hussain, C. Mangler, E. I. Kauppinen, T. Susi, J. Kotakoski, Silicon substitution in nanotubes and graphene via intermittent vacancies. *J. Phys. Chem. C* **123**, 13136–13140 (2019).

48. M. Tripathi, A. Mittelberger, N. A. Pike, C. Mangler, J. C. Meyer, M. J. Verstraete, J. Kotakoski, T. Susi, Electron-beam manipulation of silicon dopants in graphene. *Nano Lett.* **18**, 5319–5323 (2018).

49. T. Susi, D. Kepaptsoglou, Y.-C. Lin, Q. M. Ramasse, J. C. Meyer, K. Suenaga, J. Kotakoski, Towards atomically precise manipulation of 2D nanostructures in the electron microscope. *2D Materials* **4**, 042004 (2017).

50. T. Susi, J. Kotakoski, D. Kepaptsoglou, C. Mangler, T. C. Lovejoy, O. L. Krivanek, R. Zan, U. Bangert, P. Ayala, J. C. Meyer, Q. Ramasse, Silicon-carbon bond inversions driven by 60-keV electrons in graphene. *Phys. Rev. Lett.* **113**, 115501 (2014).

51. T. Susi, J. C. Meyer, J. Kotakoski, Manipulating low-dimensional materials down to the level of single atoms with electron irradiation. *Ultramicroscopy* **180**, 163–172 (2017).

52. O. Dyck, S. Kim, E. Jimenez-Izal, A. N. Alexandrova, S. V. Kalinin, S. Jesse, Building structures atom by atom via electron beam manipulation. *Small* **14**, e1801771 (2018).

53. O. Dyck, C. Zhang, P. D. Rack, J. D. Fowlkes, B. Sumpter, A. R. Lupini, S. V. Kalinin, S. Jesse, Electron-beam introduction of heteroatomic Pt–Si structures in graphene. *Carbon* **161**, 750–757 (2020).

54. X. Sang, X. Li, W. Zhao, J. Dong, C. M. Rouleau, D. B. Geohegan, F. Ding, K. Xiao, R. R. Unocic, In situ edge engineering in two-dimensional transition metal dichalcogenides. *Nat. Commun.* **9**, 2051 (2018).

55. X. Sang, X. Xie, D. E. Yilmaz, R. Lotfi, M. Alhabeb, A. Ostadhossein, B. Anasori, W. Sun, X. Li, K. Xiao, P. R. C. Kent, A. C. T. van Duin, Y. Gogotsi, R. R. Unocic, In situ atomistic insight into the growth mechanisms of single layer 2D transition metal carbides. *Nat. Commun.* **9**, 2266 (2018).

56. A. Maksov, O. Dyck, K. Wang, K. Xiao, D. B. Geohegan, B. G. Sumpter, R. K. Vasudevan, S. Jesse, S. V. Kalinin, M. Ziatdinov, Deep learning analysis of defect and phase evolution during electron beam-induced transformations in WS$_2$. *npj Comput. Mater.* **5**, 12 (2019).

57. K. Binder, J. D. Reger, Theory of orientational glasses models, concepts, simulations. *Adv. Phys.* **41**, 547–627 (1992).

58. K. Binder, A. P. Young, Spin glasses: Experimental facts, theoretical concepts, and open questions. *Rev. Mod. Phys.* **58**, 801–976 (1986).

59. A. Tagantsev, L. E. Cross, J. Fousek, *Domains in Ferroic Crystals and Thin Films* (Springer, 2010).

60. Q. He, R. Ishikawa, A. R. Lupini, L. Qiao, E. J. Moon, O. Ovchinnikov, S. J. May, M. D. Biegalski, A. Y. Borisevich, Towards 3D mapping of BO_6 octahedron rotations at perovskite heterointerfaces, unit cell by unit cell. *ACS Nano* **9**, 8412–8419 (2015).

61. M. Ziatdinov, C. Nelson, R. K. Vasudevan, D. Y. Chen, S. V. Kalinin, Building ferroelectric from the bottom up: The machine learning analysis of the atomic-scale ferroelectric distortions. *Appl. Phys. Lett.* **115**, 052902 (2019).

62. R. K. Vasudevan, M. Ziatdinov, L. Vlcek, A. N. Morozovska, E. A. Eliseev, S.-Z. Yang, Y. Gong, P. Ajayan, W. Zhou, M. F. Chisholm, S. V. Kalinin, Investigating phase transitions from local crystallographic analysis based on machine learning of atomic environments. arXiv:2006.10001 [cond-mat.mtrl-sci] (17 June 2020).

63. L. Vlcek, M. Ziatdinov, A. Maksov, A. Tselev, A. P. Baddorf, S. V. Kalinin, R. K. Vasudevan, Learning from imperfections: Predicting structure and thermodynamics from atomic imaging of fluctuations. *ACS Nano* **13**, 718–727 (2019).

64. M. Ziatdinov, O. Dyck, X. Li, B. G. Sumpter, S. Jesse, R. K. Vasudevan, S. V. Kalinin, Building and exploring libraries of atomic defects in graphene: Scanning transmission electron and scanning tunneling microscopy study. *Sci. Adv.* **5**, eaaw8989 (2019).

65. M. Ziatdinov, O. Dyck, A. Maksov, X. Li, X. Sang, K. Xiao, R. R. Unocic, R. Vasudevan, S. Jesse, S. V. Kalinin, Deep learning of atomically resolved scanning transmission electron microscopy images: Chemical identification and tracking local transformations. *ACS Nano* **11**, 12742–12752 (2017).

66. M. Ziatdinov, A. Maksov, S. V. Kalinin, Learning surface molecular structures via machine vision. *Npj Comput. Mater.* **3**, 31 (2017).

67. M. Ziatdinov, AtomAI: Deep and machine learning for atom-resolved data. *GitHub repository* (2020); https://github.com/pycroscopy/atomai.

68. M. Ziatdinov, O. Dyck, S. Jesse, S. V. Kalinin, Atomic mechanisms for the Si atom dynamics in graphene: Chemical transformations at the edge and in the bulk. *Adv. Funct. Mater.* **29**, 1904480 (2019).

69. J. Barthel, Dr. Probe: A software for high-resolution STEM image simulation. *Ultramicroscopy* **193**, 1–11 (2018).

70. T. Trevethan, C. D. Latham, M. I. Heggie, P. R. Briddon, M. J. Rayson, Vacancy diffusion and coalescence in graphene directed by defect strain fields. *Nanoscale* **6**, 2978–2986 (2014).

71. R. K. Vasudevan, M. Ziatdinov, S. Jesse, S. V. Kalinin, Phases and interfaces from real space atomically resolved data: Physics-based deep data image analysis. *Nano Lett.* **16**, 5574–5581 (2016).

72. N. Borodinov, W.-Y. Tsai, V. V. Korolkov, N. Balke, S. V. Kalinin, O. S. Ovchinnikova, Machine learning-based multidomain processing for texture-based image segmentation and analysis. *Appl. Phys. Lett.* **116**, 044103 (2020).

73. R. K. Vasudevan, A. Belianinov, A. G. Gianfrancesco, A. P. Baddorf, A. Tselev, S. V. Kalinin, S. Jesse, Big data in reciprocal space: Sliding fast Fourier transforms for determining periodicity. *Appl. Phys. Lett.* **106**, 091601 (2015).

74. A. Belianinov, Q. He, M. Kravchenko, S. Jesse, A. Borisevich, S. V. Kalinin, Identification of phases, symmetries and defects through local crystallography. *Nat. Commun.* **6**, 7801 (2015).

75. W. Lin, Q. Li, A. Belianinov, B. C. Sales, A. Sefat, Z. Gai, A. P. Baddorf, M. Pan, S. Jesse, S. V. Kalinin, Local crystallography analysis for atomically resolved scanning tunneling microscopy images. *Nanotechnology* **24**, 415707 (2013).

76. D. P. Kingma, M. Welling, Auto-encoding variational bayes. arXiv:1312.6114 [stat.ML] (20 December 2013).

77. D. P. Kingma, M. Welling, An introduction to variational autoencoders. *Found. Trends Mach. Learn.* **12**, 307–392 (2019).

78. T. Bepler, E. Zhong, K. Kelley, E. Brignole, B. Berger, Explicitly disentangling image content from translation and rotation with spatial-VAE. *Adv. Neural. Inf. Process. Syst.*, 15409–15419 (2019).

79. S. V. Kalinin, K. Kelley, R. K. Vasudevan, M. Ziatdinov, Toward decoding the relationship between domain structure and functionality in ferroelectrics via hidden latent variables. *ACS Appl. Mater. Interfaces* **13**, 1693–1703 (2021).

80. O. Dyck, S. Kim, S. V. Kalinin, S. Jesse, Mitigating e-beam-induced hydrocarbon deposition on graphene for atomic-scale scanning transmission electron microscopy studies. *J. Vac. Sci. Technol. B* **36**, 011801 (2018).

81. O. Ronneberger, P. Fischer, T. Brox, in *International Conference on Medical Image Computing and Computer-Assisted Intervention* (Springer, 2015), pp. 234–241.

82. D. P. Kingma, J. Ba, Adam: A method for stochastic optimization. arXiv:1412.6980 [cs.LG] (22 December 2014).

83. J. Gardner, G. Pleiss, K. Q. Weinberger, D. Bindel, A. G. Wilson, Gpytorch: Blackbox matrix-matrix gaussian process inference with gpu acceleration, in *Advances in Neural Information Processing Systems* (2018), pp. 7576–7586.

Citation: S. V. Kalinin, O. Dyck, S. Jesse, M. Ziatdinov, Exploring order parameters and dynamic processes in disordered systems via variational autoencoders. *Sci. Adv.* **7**, eabd5084 (2021).